Automated GNSS and Teleseismic Earthquake Inversion (AutoQuake Inversion) for Tsunami Early Warning: Retrospective and Real-Time Results

KEJIE CHEN,[1] ZHEN LIU,[2] and Y. TONY SONG[2] (iD)

Abstract—Rapid finite fault source determination is critical for reliable and robust tsunami early warnings. Near-field Global Navigation Satellite System (GNSS) observations have shown value to constrain the source inversion, but real-time GNSS stations are sparse along most of the active faults. Here we propose an automatic earthquake finite source inversion (AutoQuake Inversion) algorithm jointly using near-field (epicentral distance < 1000 km) GNSS data and mid-range (epicentral distance from 30° to 45°) teleseismic P displacement waveforms. Neither the near-field GNSS nor the mid-range teleseismic data clip or saturate during large earthquakes, while the fast-traveling P-waves are still essential to constrain the source in regions where very few or no GNSS stations are available. Real-time determination of the fault geometry remains to be the main challenge for rapid finite source inversion. We adopt a strategy to use the predefined geometry Slab2 for earthquakes within it or to forecast a focal mechanism based on near-by historical events for earthquakes without Slab2 prior. The algorithm has been implemented successfully in the prototype of JPL's GPS-Aided Tsunami Early-Detection system and tested for many real events recently. This article provides the framework of the algorithm, documents the retrospective and real-time results, and discusses remaining challenges for future improvements.

Key words: GNSS data, teleseismic data, Slab2, focal mechanism forecast, fast joint source inversion, tsunami early warning.

1. Introduction

Recent tsunami disasters induced by mega-thrust earthquakes (e.g., the 2004 Sumatra and 2011

Tohoku events) have called for the need for reliable tsunami early warning systems (TEWS), using not only the traditional seismic approach, but also Global Navigation Satellite System (GNSS). Using GNSS to estimate earthquake magnitude for tsunami early warning was first demonstrated by Geoffrey Blewitt and colleagues at the University of Nevada in Reno (Blewitt et al. 2006; Sobolev et al. 2007). Furthermore, Song (2007) demonstrated that coastal GNSS stations can be used to infer seafloor displacements and estimate earthquake-induced oceanic energy and tsunami scales within a few minutes after the quake for early warning. The GNSS approaches have been further demonstrated and improved for more earthquakes (e.g., Ohta et al. 2012; Song et al. 2012; Yang et al. 2014; Chen et al. 2016a; Fu et al. 2017).

To assess the tsunami potential and guide emergency response within minutes after a submarine earthquake, a rapid and accurate estimation of the seismic source is essential (Titov et al. 2005). Currently, most tsunami warning centers, such as the U.S. National Oceanographic and Atmospheric Administration (NOAA)'s Pacific Tsunami Warning Center (NOAA-PTWC), the local German Indonesian Tsunami Early Warning System (GITEWS) and Japan Meteorological Agency (JMA)'s tsunami warning center, use seismic network for earthquake detection, including location and source characterization (Bernard and Titov 2015). As soon as a shallow earthquake (with depth < 100 km) above threshold magnitude is found occurring under sea, tsunami alarms are then triggered and issued to target clients depending on the estimated earthquake magnitude. For example, using real time data from Federation of Digital Seismic Networks (FDSN), the U.S. Geological Survey-National Earthquake

[1] Division of Geological and Planetary Sciences, California Institute of Technology, Pasadena, CA 91125, USA.

[2] Jet Propulsion Laboratory, California Institute of Technology, Pasadena, CA 91109, USA. E-mail: Tony.Song@JPL.NASA.gov

Information Center (USGS-NEIC) is able to determine the origin time, hypocenter location and preliminary estimation of earthquake magnitude worldwide within minutes for all significant events (Hayes et al. 2011). When near-field observations are available, the procedure will take less than tens of seconds (Hoshiba et al. 2011).

While hypocenter can be located with confidence (Husen and Hardebeck 2010), traditional magnitude estimations such as M_L (Richter 1935) and M_S (Boatwright and Choy 1986) using short period seismic waves suffer from saturation for very large earthquakes (Larson et al. 2003). One such example is the underestimate of the magnitude of the 2011 M_w 9.0 Tohoku earthquake for tsunami early warning (JMA 2013). To circumvent this problem, the moment magnitude M_w, defined by Kanamori (1977), which describes total energy required to rupture the entire fault, is considered to be the most appropriate among various magnitudes for tsunami potential evaluation (Blewitt et al. 2006). Rapid determination of M_w from broadband P waveforms (M_{wp}) has been implemented in PTWC officially since 2002 (Hirshorn et al. 2013). In addition, W-phase moment tensor inversion which provides both magnitude and focal mechanism information (Kanamori and Rivera 2008) has also been performed routinely in PTWC (Duputel et al. 2011). Usually, it takes tens of minutes to stabilize a M_w magnitude estimation in such inversion (Kanamori and Rivera 2008; Hayes et al. 2011).

Traditionally, TEWS have been relying on earthquake magnitude to issue tsunami alert or warning levels. While it is true that a larger earthquake magnitude usually indicates a greater tsunami potential, the historical tsunami maximum water heights and earthquake magnitudes show a much more complex correlation between the two (see Fig. 1). For example, with respect to the $M_w \sim 8$ earthquakes, the tsunami maximum water heights vary from less than 3 m to more than 30 m, which poses a challenge for tsunami early warning and suggests that the point source magnitude used in current TEWS needs improvements. Sensitivity analysis conducted by Titov et al. (1999) showed that point source model provides an essential description of far-field tsunami signals. As a result, the NOAA

system has been providing regional (distance larger than 1000 km) warnings routinely with success. However, for a local tsunami near Padang of Sumatra Island, Sobolev et al. (2007) demonstrated that different distribution of slip could generate totally different impacts on coastal wave heights in spite of the same magnitude and location. In addition, Weinstein and Lundgren (2008) acknowledged the challenges the warning centers faced when coping with unusual earthquakes (such as 2001 M_w 8.4 Peru, 2004 M_w 9.3 Sumatra, 2006 M_w 7.7 Java), and concluded that improved tsunami wave-height forecasts would be achieved if considering the slip distribution along a fault. Indeed, recent studies of Song et al. (2008, 2017) found that what really matters is not the earthquake magnitude alone. Instead, the size and power of a tsunami depend on the amount of energy transferred to the ocean by the earthquake-induced seafloor displacements. Based on the energy principle, Song (2007) proposed a method for estimating the tsunami energy directly from coastal GNSS stations near the epicenter. More recently, Inazu et al. (2016) developed a near-field TEWS using an automatic CMT estimation, their results showed increasing forecast uncertainties for larger ($M_w > 8$) earthquakes because the tsunami source cannot be treated as a point any more. In a retrospective real-time analysis of the 2011 Tohoku event, Melgar and Bock (2015) highlighted the importance of a reliable finite slip model through a detailed comparison of predicted tsunami's inundation and survey measurements. However, real-time GNSS sites along coastal regions are often not dense enough to provide reliable estimation of the seafloor displacements. So far, many aforementioned GNSS approaches and related publications are based on post-event processed data and implementation. To our knowledge, real-time inversion of earthquakes just using GNSS is only feasible in regions where there is a dense GNSS network (Kawamoto et al. 2016, 2017), while a global GNSS-based earthquake source inversion system has never been reported except post-event demonstration in simulated environment.

To resolve the data sparse problem of real-time GNSS sites along coastal regions, we propose an automated joint inversion based on near-field (< 1000 km) GNSS data and mid-range (epicentral
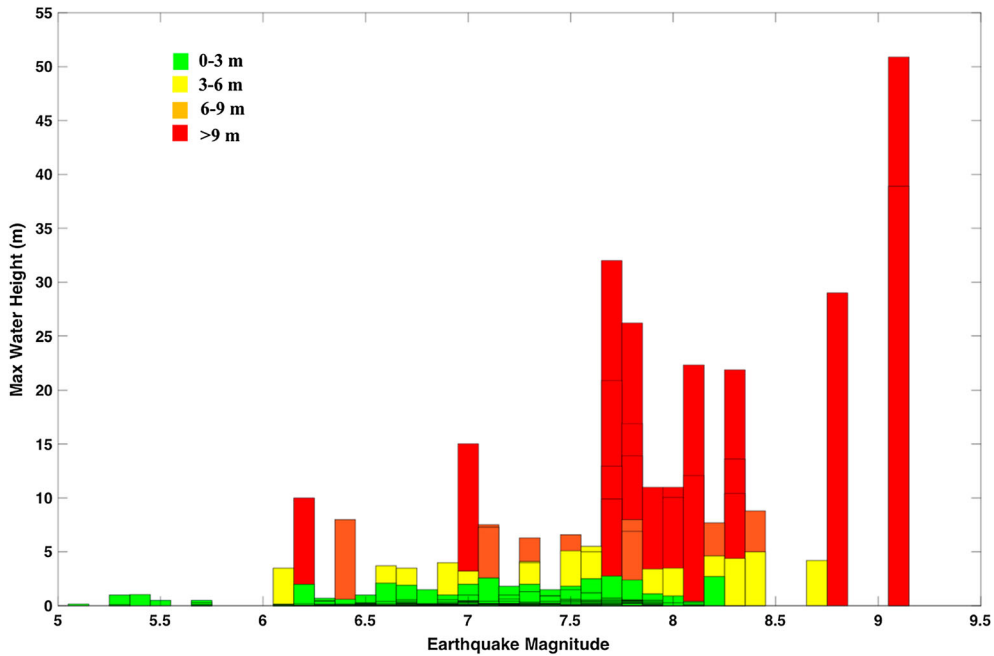
Figure 1
Historical earthquake magnitude and corresponding tsunami maximum water height since 1985. Records are from NOAA tsunami database. Maximum water heights are either runups or buoy records, depending on data availability. Data source: https://www.ngdc.noaa.gov/nndc/struts/form?t=101650&s=166&d=166

distance ranging from 30° to 45°) teleseismic P displacement waveforms. In fact, teleseismic P displacement waveforms, within $6 \sim 8$ min away from the epicenter, are still essential to constrain the source in regions where near-field GNSS data are not dense enough. The global deployment of FDSN stations provides publicly available seismic records for all large earthquakes with extensive epicentral distance and azimuthal distributions. In fact, teleseismic P waveforms are among the first datasets proposed to investigate earthquake finite source features in the context of tsunami early warning (e.g., Weinstein and Lundgren 2008; Mendoza and Hartzell 2013). Meanwhile, advances in GNSS have made it possible to measure both static and kinematic ground motions at mm-cm level in real-time without clip (e.g., Bock et al. 2000; Li et al. 2013; Liu et al. 2014; Chen et al. 2016b; Geng et al. 2017). Especially, real-time high-rate ($\geq$ 1 Hz) GNSS has made the boundary between geodetic and seismic sensors blurry. Compared with teleseismic data, GNSS derived kinematic co-seismic signals are more favored for source studies of large

earthquakes because of higher spatial–temporal resolution (Yue and Lay 2013).

Besides the real-time data availability issues, other challenges still exist for fast earthquake finite source inversion. One major difficulty is the instant determination of fault geometry. Finite source inversion needs predefined fault geometries, which are traditionally obtained from point-source moment tensor inversions (Kanamori and Rivera 2008). Moment tensor inversions usually rely on long period seismic waveforms, which may have a large latency ($20 \sim 30$ min). GNSS data have been suggested to estimate the moment tensor or earthquake magnitude by peak ground displacements estimation recently (e.g., Crowell et al. 2012; Melgar et al. 2016), but obtaining sufficient data in real-time is still a challenge globally. Besides, moment tensor solution provides two conjugated planes. Resolving fault plane ambiguity requires additional efforts.

In the following section, we first describe our real-time data source and streaming, and then present approach to deal with fault geometry and finite source

inversion strategy. In Sect. 3, we assess the algorithm through both retrospective and real-time analyses of five events in different tectonic settings. We then summarize our work and discuss future improvements to make our system more robust and efficient in Sect. 4. Supplemental materials are provided online.

2. Data and Methods

2.1. Real-Time GNSS and Teleseismic Networks

In this study, we use real-time GNSS data from NASA Global Differential GPS (GDGPS) network, which provides the operationally robust and self-sustainable front-end required for a global natural hazard monitoring system (www.gdgps.net). It is a high-accuracy, high-reliability, 24/7 GNSS augmentation system, developed by JPL to support the real-time positioning, timing, and orbit determination requirements of its customers at NASA, the Air Force, and in industry. By using accurate real-time orbit and clock products, NASA GDGPS employs precise point positioning to estimate site coordinates, which ensures the solutions can be obtained in real time. In order to improve robustness of the system, data filtering and quality control are also applied to the real-time co-seismic displacement waveforms. We are streaming the 1 Hz positioning time series with few centimeters' accuracy for about eight hundred of GNSS continuous tracking stations (see their distribution in Fig. 2) from both regional and global networks, recording ground dynamic displacements right before, during and after earthquakes routinely. In addition, static co-seismic offsets are estimated automatically in near real-time (seconds to minutes latency) from high-rate GNSS displacement waveforms using the methodology by Liu et al. (2014). The near field GNSS stations are subject to coseismic displacement influence when epicentral distance is within $10^{(M/2-0.8)}$ km where M is earthquake magnitude (http://geodesy.unr.edu/). For the megathrust event like the 2011 M_w 9.0 Tohoku earthquake, GNSS stations as far as 3000 km away can experience co-seismic shaking. To avoid long latency associated with far field stations, which can take tens

of minutes due to dynamic wave propagation and settlement, in our real-time system we consider only GNSS stations within 1000 km to the epicenter.

As mentioned above, near-field seismograms can saturate during strong shaking caused by large earthquakes. Teleseismic P and S waves are separated from other phases at far-field epicentral distance ($\geq 30°$) and usually used to image earthquake source. Compared with P waves, S waves travel at a relatively slow speed and may delay the system's response. Besides, automated picking of S waves is more challenging. As a result, we adopt teleseismic P waveforms from Global Seismographic Network (GSN) due to its stable real-time access in our system (see station distribution in Fig. 2). Specially, to speed up response time, we require the station epicentral distance to be between 30° and 45°. We remove the instrument response by deconvolution. The sampling rates of the original waveforms are usually larger than 20 Hz. However, this high-frequency information of observations cannot be precisely modeled because of the limitation in 3-D velocity model and inaccuracy of 1-D velocity model. We thus decimate the raw observations to 1 Hz and bandpass filter them with [0.009, 0.4] Hz. We perform the same operation on the synthetic Green's functions. We limit the P wave windows to 120 s enclosing earthquake and expected P wave arrival time. The selected P wave windows could have some contamination from PP wave arrivals for stations at shorter epicentral distances. We neglect the contaminated tail energy after the P wave phase.

Compared with teleseismic stations, the near field GNSS receivers (< 1000 km) have much less latency to get co-seismic signals with just a few seconds data transmission time and provide better constraints on slip distribution. Therefore, in the system we give GNSS data higher priority. If we have more than seven GNSS stations (note that the number seven is quite arbitrary, as it will be discussed later), we will carry out the GNSS inversion. Otherwise, we will include seismic data. The joint usage of GNSS and seismic data raises the issue of relative weighting. This is an ongoing research topic and no thumb of rule exists yet. The trial-and-error method that is frequently used is not suitable for a real-time implementation. Here, we normalize each data type
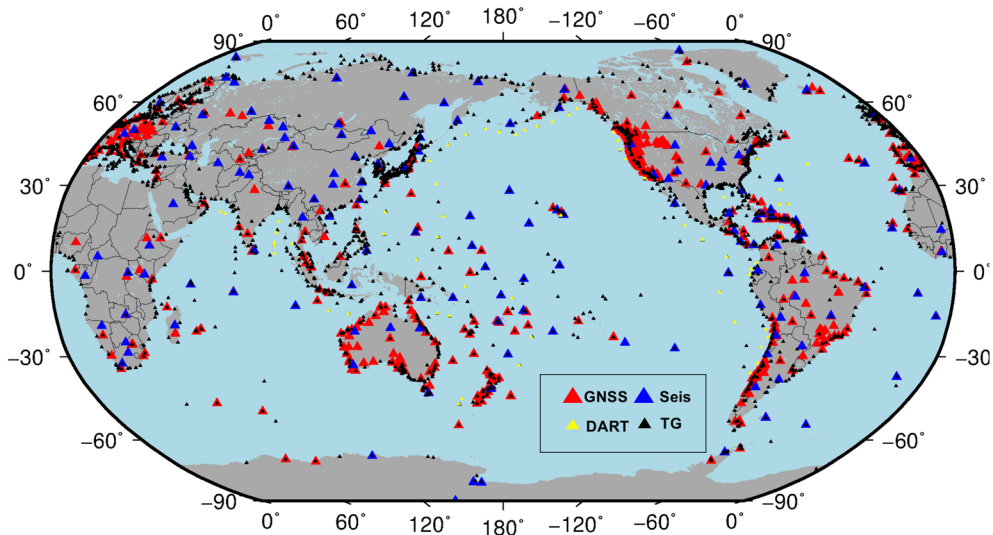
Figure 2
Distribution of real-time GNSS stations processed by JPL (red triangle), global seismograph network (blue triangle), DART buoys (smaller yellow triangle) and tide gauges (smaller black triangle)

by its own norm on a station basis and assign equal weights to them.

2.2. Fault Geometry Determination

When modeling an earthquake rupture, inverting heterogeneous slip distribution and fault geometry simultaneously will be nonlinear and intractable. In most cases, we assume a prefixed fault plane in the source region, which is usually discretized into a number of subfaults in the source region. To define the fault plane geometry, seven parameters are needed: the position of reference point (longitude, latitude, and depth), the size (length and width), and the orientation (strike and dip angles). In our system, we set the hypocenter location as the center point (or reference point) of fault plane. With respect to the size, we follow the empirical magnitude-area scaling relationships developed by Wells and Coppersmith (1994). Note that we do not know whether the earthquake is unilateral or bilateral, and the initial seismically estimated magnitude tends to be underestimated. We thus set the source fault dimension large enough to accommodate rupture in either direction. Specially, for $M \geq 7.5$ earthquakes, we set the rupture length as 400 km and width as

200 km. The fault is then subdivided into 20 along-strike and 10-along dip segments.

In addition, we also need to constrain rake angle range to stabilize the inversion results. Strike, dip and rake angles, usually provided as part of focal mechanism, are traditionally derived from centroid moment tensor solution. Currently, focal mechanisms for significant earthquakes are routinely provided by several international organizations (e.g., GCMT, USGS, GFZ) with latencies from tens of minutes to hours. Recently, algorithms based on local and regional GNSS observations are also proposed to speed up the determination of centroid moment tensors (Melgar et al. 2012; Riquelme et al. 2016). However, as mentioned above, real-time availability of GNSS data may severely limit the algorithms' performance for an operational system. Furthermore, focal mechanism solution contains two conjugated nodal planes, and more times are required to resolve nodal plane ambiguity for finite source inversion, which further delays emergency response.

Based on the catalogues of the historic seismicity, bathymetry and gravity data sets, a global subduction zone geometry model called Slab1.0 has been developed (Hayes and Wald 2009; Hayes et al. 2012). Slab1.0 outlines three-dimensional geometry

of almost 80% of subduction zones over the world. More recently, Slab1.0 was updated and extended to Slab2 (available at https://github.com/usgs/slab2, also see Fig. 3a), which covers $\sim$ 30% more than Slab1.0 (Hayes et al. 2018). To evaluate its potential to constrain fault geometry in finite source inversion for TEWS, we first checked fault strike orientations inferred from Slab2 and GCMT solutions. From January 1976 to December 2017, GCMT catalog recorded totally 543 $M_w \geq 7.0$ earthquakes (see their distribution in Fig. 3), among them are 370 submarine events with epicenter depth less than 100 km, and 272 of the 370 events are within Slab2 zone coverage. Figure 3 indicates that Slab2 strike orientation agree with GCMT solution quite well. To quantify their consistency, we adopt the criterion proposed by Kagan (1991) (hereafter referred to as Kagan angle). Kagan angle measures differences between the orientations of two seismic moment tensors, it varies from 0° to 120°, and two focal mechanisms are considered to be very similar when the Kagan angle is less than 30° (Kubo et al. 2002). Note that Slab2 is a subduction model, we treat all of these earthquakes as thrusting events with 90° rake angle. The results of comparisons (see Fig. 3b) show

that $\sim$ 63% of strike angles in GCMT solutions are within 30° Kagan angle against their Slab2 values, $\sim$ 83% are within 40° and $\sim$ 90% are within 50° Kagan angle, which indicates Slab2 is a good representation of fault geometry for mega-thrust subduction earthquakes. Encouragingly, the consistency between Slab2 and GCMT solution increases as the earthquake magnitude grows (see Fig. 3c), and the Kagan angles are within 40° for all $M_w > 8$ earthquakes. Here, we incorporate Slab2 as fault geometry priors to perform finite source inversion in our system. In practice, immediately after the hypocenter is provided, we begin to search Slab2 database to extract fault geometry. Ideally, for an inter-plate thrust faulting earthquake that takes place in Slab2, its hypocenter depth and corresponding Slab2 depth should be close to each other. Otherwise, even the epicenter falls in the horizontal projection (Fig. 3a) of the Slab2, the earthquake could be another type of faulting, such as intra-plate normal faulting (e.g., the 2018 M_w 8.2 Mexico Tehuantepec earthquake) or back-arc thrust faulting (e.g., the 2018 M_w 7.0 Lombok earthquake discussed later in this paper). To that end, we adopt the depth difference between hypocenter and Slab2 as a criterion to decide
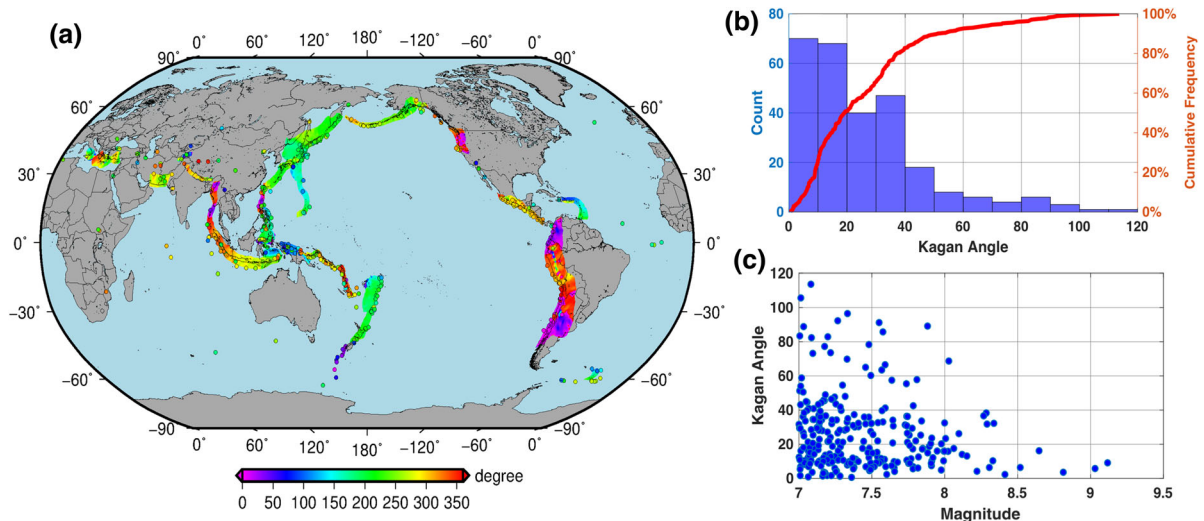

Figure 3

a Strike angles of $M_w > 7$ earthquakes in GCMT from 1976 to 2017 (represented by circles) and that inferred from Slab2 (color). Note that original GCMT solutions provides two strike angles for the two nodal planes, we chose the one closer to Slab2. The strike angle is indicated by the color scale. **b** Histogram and cumulative frequency of similarity between GCMT solutions and Slab2 priors for 272 $M_w \geq 7$ earthquakes in subduction zone. **c** Kagan angle versus earthquake magnitude

whether we can use Slab2-inferrd fault geometry for source inversion. Considering the fact that the hypocenter depth and Slab2 depth can differ up to tens of kilometers within uncertainties, we currently set the threshold of depth difference as 30 km.

Neighboring large earthquakes, if they fall within the same tectonic settings, usually have similar focal mechanisms, suggesting that it is possible to forecast mechanisms of future earthquakes based on nearby historical events (Kagan and Jackson 1994). As a matter of fact, Kagan and Jackson (1994) proposed an interpolation algorithm to predict focal mechanism considering factors such as epicentral distance, magnitude and directivity. Inspired by their ideas, we infer the fault geometries for those earthquakes out of Slab2 by interpolating neighboring $M_w > 5$ historical events (see Fig. S1) as the forecasted focal mechanisms (see Fig. 4a). We validated the predictions by comparing 98 historical earthquakes with $M_w > 7$ against their forecasted values. The comparison statistics show that $\sim 75\%$ of them are within $30°$ Kagan angle, $\sim 80\%$ are within $40°$ Kagan angle (Fig. 4b), and the consistency further improves for larger events (Fig. 4c). These results agree well with Slab2. Of particular note, the forecasted focal mechanism contains two nodal planes, and we run two

groups of finite source inversion in parallel to find the favorable one based on the data fits.

2.3. Rapid Joint Finite Source Inversion

Finite source inversion can be either static (using permanent offsets) or kinematic (using waveforms). Modelling waveforms can be more time-consuming than static inversion because more record samplings are utilized. Besides, based on our real-time tests, we find that data loss and discontinuity make the kinematic inversion based on high-rate GNSS complicated. As a result, if there are enough (> 7) GNSS offsets with good azimuthal coverage (the epicenter-station azimuth range $> 90°$) available, we will perform only static inversion to get slip distribution. Note that using station number > 7 and azimuth coverage $> 90°$ as criteria for enough GNSS stations is a bit subjective, but our results have shown that it is able to provide acceptable tsunami forecast for early warning. When GNSS observations are insufficient or absent, we switch to kinematic source inversion based on teleseismic P waveforms and GNSS offsets. To this end, we use the linear multi-time window approach (Ide et al. 1996) with a rupture velocity as 80% of the shear wave speed (Bilek and Lay 1999). However, for "tsunami earthquakes" which generate
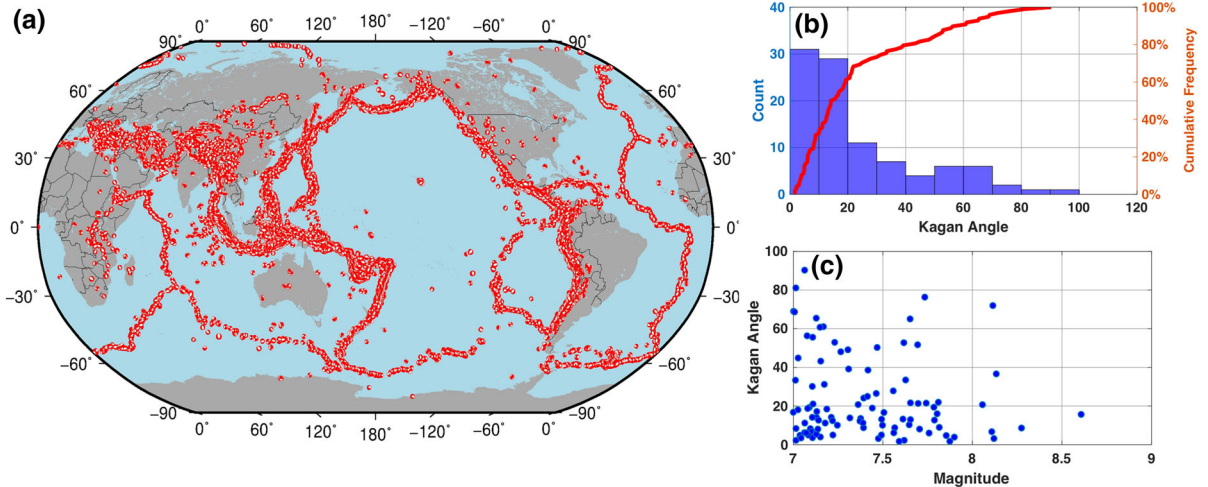

Figure 4
a Focal mechanism forecast based on GCMT catalog from January 1976 to December 2017. Focal mechanisms are shown on $2° \times 2°$ grid. **b** Histogram and cumulative frequency of similarity between GCMT solutions and forecast focal mechanism for 98 $M \geq 7$ earthquakes without Slab2 priors. **c** Kagan angle against magnitude

tsunamis much larger than expected based on their magnitudes (Kanamori 1972), the rupture velocity can be as slow as 1.0–1.5 km/s, like the 17 July 2006 M_w 7.7 Java (Ammon et al. 2006) or the 25 October 2010 M_w 7.8 Mentawai (Yue et al. 2014) earthquake. Usually we run iterations with a group of different rupture velocities to identify the reasonable one based on the corresponding data misfits. Unfortunately, teleseismic P waves are less sensitive to the change of rupture velocity, therefore we only run the iteration when GNSS data are included. Furthermore, the choice of window number, rise time length is quite arbitrary. Here, we assume five 4 s long triangle source time functions with 50% overlapping at each sub-fault.

We use frequency wavenumber integration approach (Zhu and Rivera 2002) to calculate Green's functions (GFs) for static GNSS based on the 1-D rigidity structure CRUST 2.0 (http://igppweb.ucsd. edu/~gabi/crust2.html) at the source, and the GFs are computed from 0 to 0.5 Hz for every sub-fault/ station pair. The teleseismic Green's functions are generated with a propagator matrix approach (Kiku-chi and Kanamori 1982). We adopt CRUST 2.0 for the source side and preliminary reference earth model (PREM) (Dziewonski and Anderson 1981) for the receiver side. Slip distribution inversion is usually an ill-posed problem. To ensure stability, for static source inversion, we employ Laplacian regularization (Hartzell and Heaton 1983) to constrain the total slip at each sub-fault. For multi-window kinematic source inversion, an additional constraint on the amplitude of the neighboring time windows at each sub-fault is added. In this case, we will have both spatial and temporal smoothing factors to be defined. To mini-mize manual intervention for determination of the optimal regularization values, we run a total of 25 iterations with gradually increasing spatiotemporal smoothing levels and then use the formalism of Akaike's Bayesian Information Criterion (ABIC) (Akaike 1980) to select the most favorable smoothing pair.

2.4. Tsunami Validation

We use the open source code GeoClaw (http://clawpack.org) for tsunami simulation. To be specific,

we first derive horizontal and vertical sea floor deformation following the planar fault model of Okada (1985), and then obtain total deformation by summing the vertical motion and the vertical com-ponent caused by the advection of topography in horizontal directions (Tanioka and Satake 1996). After that, we take the total deformation as an initial condition for a model run and the simulation is conducted by including topography and bathymetry data sets with 15 arc second resolution (Becker et al. 2009). To validate the slip model, we then compare the model-predicted tsunamis with either tsunami run-up measurements or tsunami waves at coastal tide gauges, depending on the data availability. We also run tsunami simulation based on published post-event models by other researchers, To further assess the performance and advantage of our system in the context TEWS, we also run tsunami simulations based on sea floor deformation derived from the currently used standard centroid moment tensor solutions using the so called Rupture Generator developed by Babeyko et al. (2010).

The algorithm has been implemented successfully in the prototype of JPL's GPS-Aided Tsunami Early-Detection (GATED) system. Earthquake hypocenter, origin and initial magnitude are provided by USGS, and NOAA TWCs through operational global seismic network detections (earthquake alert), which trigger our system, and the entire workflow for our system is shown in Fig. 5. Of particular note, considering the initial reported hypocenter depth can be very inac-curate, we use the Slab2 interface depth to construct the finite fault.

3. Results of Illustrative Case Studies

To evaluate the performance of our automated GNSS and telesiesmic inversion algorithm, we have implemented the algorithm into JPL's GATED sys-tem, and simulated a number of historical large earthquakes ($M \geq 7$) in retrospective mode and pro-cessed some moderate earthquakes ($M > 6.5$) in real time. Here we present the results as summarized in Table 1 and evaluate their uncertainties against observations and well-studied published source models as well. The input datasets are either near-
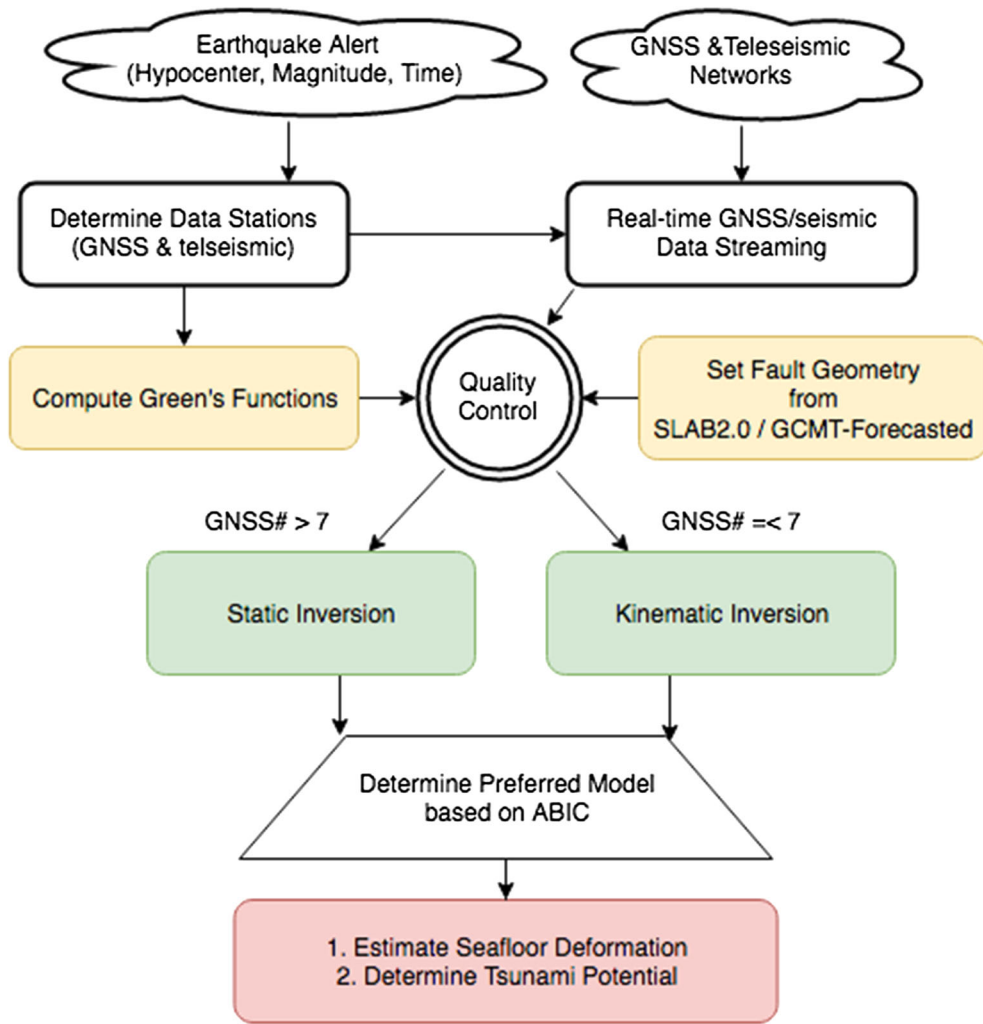
Figure 5
Flowchart of automated GNSS and teleseismic earthquake finite source inversion (AutoQuake Inversion) algorithm implemented at JPL

Table 1

Summary of the AutoQuake inversion in retrospective or real-time mode

Earthquake	Fault geometry	Datasets	Time (min)
2011 M_w 9.0 Tohoku	Slab2	GNSS	∼ 7
2015 M_w 8.3 Illapel	Slab2	GNSS + P waveforms	∼ 13
2016 M_w 7.8 Solomon Island	Slab2	P waveforms	∼ 12
2016 M_w 7.8 Kaikoura	Forecasted focal mechanisms	GNSS	∼ 2
2018 M_w 7.0 Lombok	Forecasted focal mechanisms	P waveforms	∼ 14

The time is based on a computer with Intel Xeon processor and 2.5 GHz CPU (16 GB RAM)

field GNSS offsets or mid-range teleseismic P waveforms or both, accurate or inaccurate fault geometries are inferred from Slab2 or forecasted focal mechanisms, which covers all possible operational scenarios.

3.1. The 11 March 2011 M_w 9.0 Tohoku Event

The 11 March 2011 M_w 9.0 Tohoku earthquake generated one of the most powerful and devastating tsunamis in history, which caused more than 15,000 deaths and huge social and economic losses. Meanwhile, it is also one of the ever best GNSS observed mega-thrust events. As aforementioned, we currently do not have the real-time GNSS data from Japan streamed to our system. Note that this event provides an ideal opportunity to test the performance of GNSS-only-based automatic finite source inversion, we replay automatic source inversion in simulated real-time scenario. Totally 801 GNSS stations from GEONET within 1000 km epicentral distances are adopted.

Fault geometry from Slab2 yields a strike angle as 191°, dip angle as 15° at the hypocenter location, very close to the GCMT solution (strike 203°, dip 10°, rake 88°, M_w 9.1). With respect to the earthquakes happening in Slab2, as mentioned above, we assume they are thrusting events and slip vectors are within rake 45° and 135° angles for each fault, which ensures a thrusting rupture but allows strike components in a non-negative least square inversion.

Automatically-derived slip from the 801 GNSS stations are shown in Fig. 6a. The fit to the GNSS data has a variance reduction (VR) as high as 92%, which indicates that a single plane can represent the overall fault geometries quite well. The largest slip is up to 52 m, and the rupture area covers approximately 250 km along the trench. While major slips concentrate around (38°N, 143°E), slip also extends to the south, which can be interpreted as a second asperity to some extent. The total seismic moment released by the main shock is about 4.1×10^{23} Nm from finite slip inversion, equivalent to M_w 9.0, slightly smaller than the GCMT solution. Besides, the centroid location of the finite slip is about 30 km north to the GCMT solution. Of special importance, the GNSS-based inversion shows a very large and shallow (less than 20 km) slip distribution, which accounts for the huge seafloor deformation and tsunami ensuing from the earthquake.

The simulated maximum tsunami runups from our fast finite slip, Yue and Lay (2013)'s slip model inverted from high-rate GNSS and seismic waveforms, and centroid moment along the coast are shown in Fig. 6b together with the observations. Generally, our finite slip model predicted tsunamis show a good agreement with the records and can be used to decide proper warning levels within minutes after the earthquake. For coastal run-ups, variance reductions between observations and predictions are $\sim$ 80% south of 39°N, which suggests that the major slip distribution around (38°N, 143.25°E) from GNSS offsets is reasonable. However, the runup magnitude is systematically underestimated north of 39°N, indicating that an additional tsunamigenic source may be missing. In fact, many other source models, also present similar mismatches (MacInnes et al. 2013). Tappin et al. (2014) suggests a submarine mass failure (e.g., a submarine landslide) likely contributes to the tsunami as well. However, using the same GNSS data for the seafloor deformation based on Song et al. (2012), Titov et al. (2016) shows that the NOAA tsunami model agrees well with the run-ups data available along the Japanese coast and the Hawaii coast. The major difference is that they included the horizontal force due to the impulses of the faulting continental slope in the tsunami source, as described in Song et al. (2008). Currently, the GeoClaw model does not have the capability to include the horizontal force for tsunami simulation. Modifying the GeoGlaw model is beyond the scope of this work. Nevertheless, the current GeoClaw model serves well for our purpose to quantify our automated finite source inversion algorithm. For example, the GeoGlaw shows quite different tsunami results from our finite source (red in Fig. 6b) and the CMT solution (blue in Fig. 6b), in which the latter fails to characterize the amplitude of the tsunami. In fact, the tsunami amplitude is the most important factor to determine tsunami force and destructiveness for early warning.
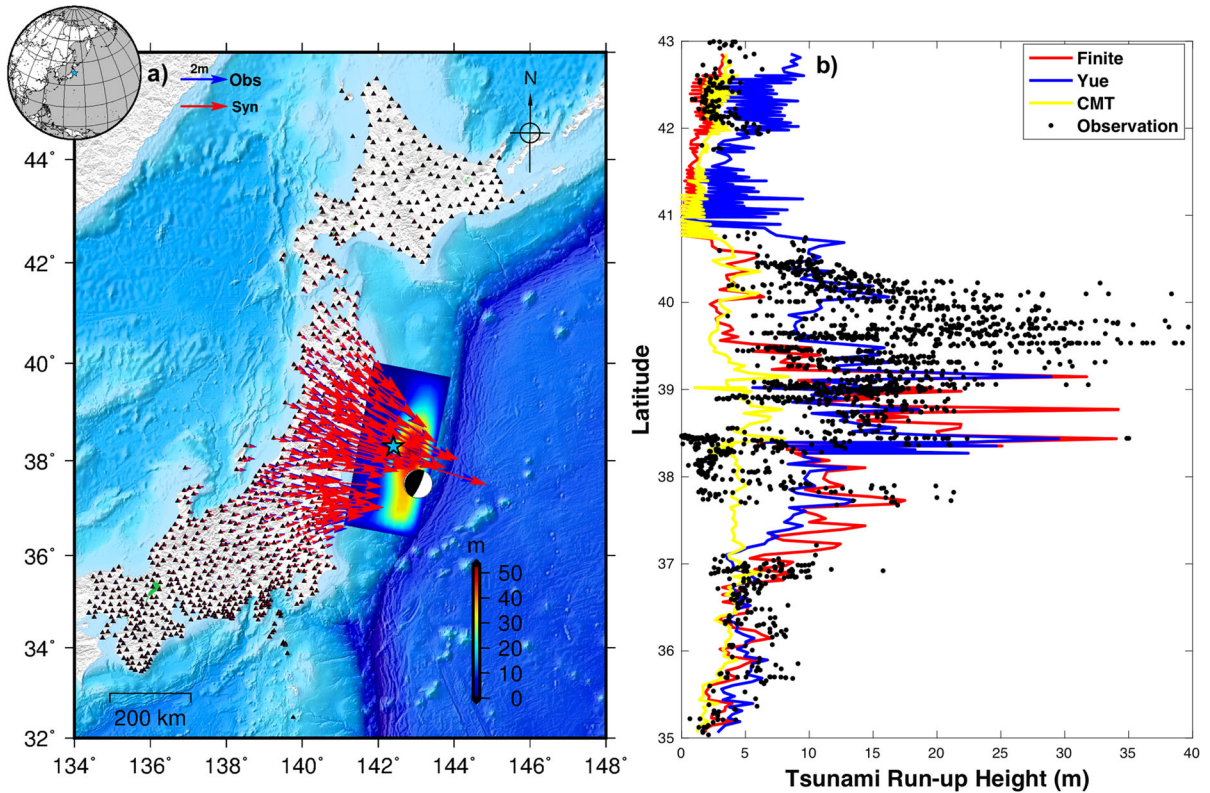
Figure 6

a Co-seismic slip distribution and GNSS data fits for the 2011 M_w 9.0 Japan Tohoku earthquake. The blue star and black beachball denote the preliminary epicenter provided by USGS and GCMT centroid moment, and blue and red vectors are observations and synthetics, respectively. **b** Tsunami run-up height predictions based on our fast co-seismic slip inversion (red), Yue and Lay (2013)'s inversion (blue) using high-rate GNSS and seismic waveforms, and GCMT solution (yellow), run-up observations (black) were provided by Mori et al. (2011)

3.2. The 16 September 2015 M_w 8.3 Illapel Event

As one of the world's most seismically active regions, continuous GNSS network has been deployed in Chile since the early 1990s by several international groups to monitor geodynamics. Following the 2010 M_w 8.8 Maule earthquake, the GNSS network has been improved greatly by increasing spatial density and reducing solution latency, which will also benefit earthquake and tsunami early warnings (Báez et al. 2018). To date, real-time GNSS data at a few stations are streamed to our system. The 16 September 2015 M_w 8.3 Illapel earthquake produced a maximum 11 m local tsunami run-up and all coastal residents (about one million people) were warned to evacuate by Chilean National Emergency Management Office. However, when the

evacuation was ordered, it did not contain any information on the tsunami intensity forecast, and it turns out that the tsunami damages were quite localized. Whereas failing to evacuate can cause loss of life, false alarm can undermine the credibility of warning system lead to poor response to future warnings.

For this event, co-seismic offsets at only three GNSS stations are available in our system. As a result, we also included P waves at 11 teleseismic stations (see their distribution in Fig. S2). Strike/dip angles inferred from Slab2 are 7°/15° based on the preliminary hypocenter location, close to the GCMT solution (strike/dip/rake as 7°/19°/109°). Since this is a joint kinematic source inversion, we run iterations using rupture velocities ranging from 1.0 km/s to 3.5 km/s with a step as 0.5 km/s. It turns out that a
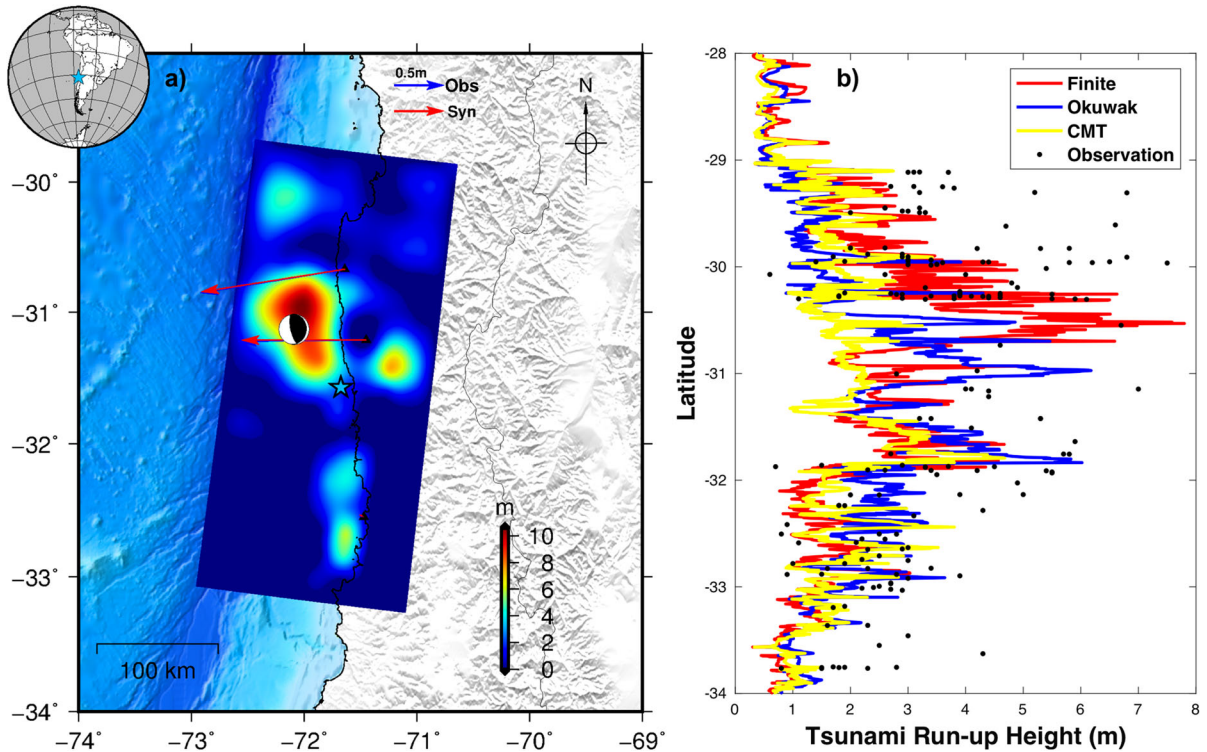
Figure 7

a Slip distribution inverted from GNSS offsets and teleseismic waveforms for the 2015 M_w 8.3 Chile Illapel earthquake. Blue star locates USGS epicenter and beachball denotes GCMT solution, blue are red vectors and observations and fits, respectively. Fits for teleseismic waveforms are shown in Fig. S2. **b** Tsunami run-up predictions from our fast finite source inversion (red), Okuwaki et al. (2016)'s inversion using P waveforms which was constrained by back-projection, and GCMT solution (yellow). Run-up observations (black) were provided by Contreras-López et al. (2016)

rupture velocity of 2.0 km/s gives the minimum misfit of GNSS data and the corresponding slip model (see in Fig. 7a) shows this earthquake ruptured bilaterally along strike, the peak slip reaches about 11 m. The majority asperity occurred about 70 km northwest to the epicenter and consistent with the GCMT centroid location. Besides, there is also a smaller but much shallower rupture asperity. Tsunami runups predicted from the slip model (see in Fig. 7b) indicate a major warning zone from $\sim$ 29.5°S to $\sim$ 32.9°S with the most affected area from $\sim$ 30.2°S to $\sim$ 30.6°S, almost identical with the observations. By contrast, the point source centroid solution fails to forecast the tsunami intensive zone.

3.3. The 8 December 2016 M_w 7.8 Solomon Island Event

Unlike the 2011 M_w 9.0 and 2015 M_w 8.3 Illapel events, we do not have any GNSS data or other nearby observations to constrain finite source inversion for the 8 December 2016 M_w 7.8 Solomon Island earthquake, only teleseismic P waves can be utilized. Worse still, the fault geometry is not very accurate: The Slab2 at hypocenter location indicates strike as 306°, dip as 28°, whereas GCMT solutions shows the strike and dip are 285°, dip 50°, respectively. Besides, the GCMT rake angle is 57°, indicating that thrust components are not overwhelmingly dominant. Tsunami warnings were issued immediately after the earthquake based on its magnitude. However, according to the sea level gauges, the largest observed wave was only around 0.1 m. Here we take it as an
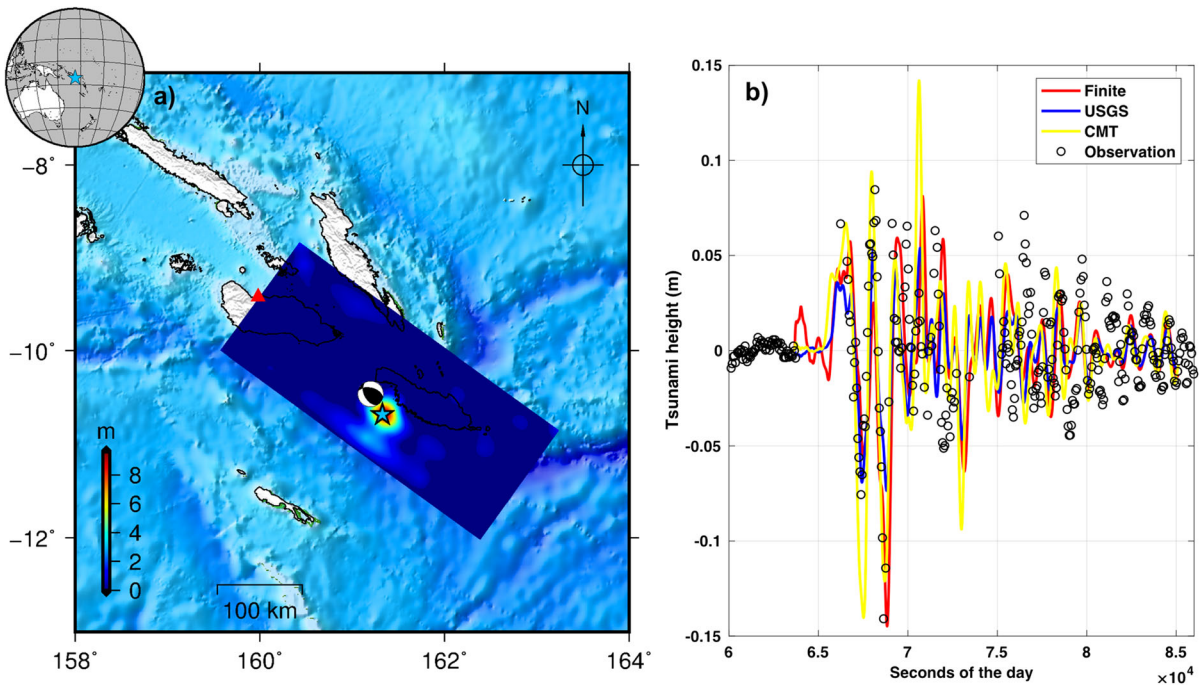
Figure 8

a Slip distribution of the 2016 M_w 7.8 Solomon Island earthquake inverted from teleseismic waveforms based on fault geometry inferred from Slab2, blue star and black beachball show USGS epicenter and GCMT solution, the red triangle is the location of tide gauge SOLO. **b** Predicted tsunamis waves from our fast finite source inversion (red), USGS model (https://earthquake.usgs.gov/earthquakes/eventpage/us20007z80/finite-fault) using P and S waveforms (blue), and GCMT solution (yellow) at coastal tide gauge SOLO. Note that later arriving tsunamis cannot be well modeled due to complex interactions between the coast and shallow bathymetry. Tsunami observations (black) were provided by Global Sea Level Observing System

example to test the system performance under adverse circumstance. The overall P waveform fits are not very good (Fig. S3, VR = 45%), only four stations show pleasant matches between observations and synthetics. The preferred model (Fig. 8a) favors a compact slip around the hypocenter, which is consistent with the P waves. Encouragingly, the predicted tsunami wave (Fig. 8b) at coastal tide gauge re-produce the measurements reliably, the maximum 0.12 m tsunami height indicates a negligible tsunami risk and evacuation to higher land is not required.

We also conducted slip inversion based on the GCMT fault geometry (Fig. S3), while the data fits improve obviously (VR = 82%), the slip distribution remains compact around the epicenter, and corresponding tsunami waves show slight differences compared with result inferred from Slab2 geometry (Fig. 9b). Inaccurate fault geometry increases

uncertainties of earthquake source estimation, but still reliable for tsunami early warning.

3.4. The 13 November 2016 M_w 7.8 Kaikoura Event

The earthquakes modelled above are well represented by a single fault. However, earthquake ruptures can be much more complex. For example, as one of the most complicated events ever instrumentally recorded (Hamling et al. 2017), the 2016 M_w 7.8 Kaikoura earthquake in New Zealand ruptured across more than 12 disparate faults with varying focal mechanisms, which raises the question of whether such a complex earthquake can be modeled automatically with confidence to guide tsunami response in real time. To investigate this problem, here we present a retrospective analysis of the Kaikoura earthquake inversion using GNSS offsets. Specially, there is no a priori fault geometry

from Slab2, and we inferred the fault geometry based on the forecasted focal mechanisms with strike/dip/rake as 238°/50°/170°, together with an auxiliary plane as 324°/87°/53°. Note that GCMT solution of for the M_w 7.8 Kaikoura event are 226°/33°/141°.

We run inversions based on both nodal planes to identify the preferred fault geometry. Data fits of the fault plane 238°/50°/170° show VR as 52% and is significantly better than fault plane 238°/50°/170° with VR as 31%. The selected slip model and tide gauge predictions are shown in Fig. 9a. The rupture features a maximum slip of ∼ 11 m, roughly 110 km northeast of the epicenter, very close to the GCMT centroid location. The derived magnitude is M_w 8.2, which overestimates the magnitude by 0.4 magnitude units compared with the GCMT solution. With respect to the tsunami observations, we find that even just based on a single fault, there is a remarkably good agreement between the predicted and recorded maximum tsunami amplitudes at near-field the tide gauges (see Fig. 9b), even though the far-field tsunamis are a bit amplified. In fact, Bai et al. (2017) showed that two regions of co-seismic seafloor deformation produced the tsunami, of which include a transpressional crustal faulting reaching offshore near Cook Strait, and that is consistent with our main slip patch.

We also synthetized tsunami waves using GCMT solution, and find its fit to amplitude at the nearest tide gauge KAIT is relatively poor, which could be caused by the underestimation of tsunamigenic slip (undersea slip) when expanding the centroid point solution to finite fault. We conclude that for rapid near-field tsunami amplitudes forecasting, even though the single fault model does not account for
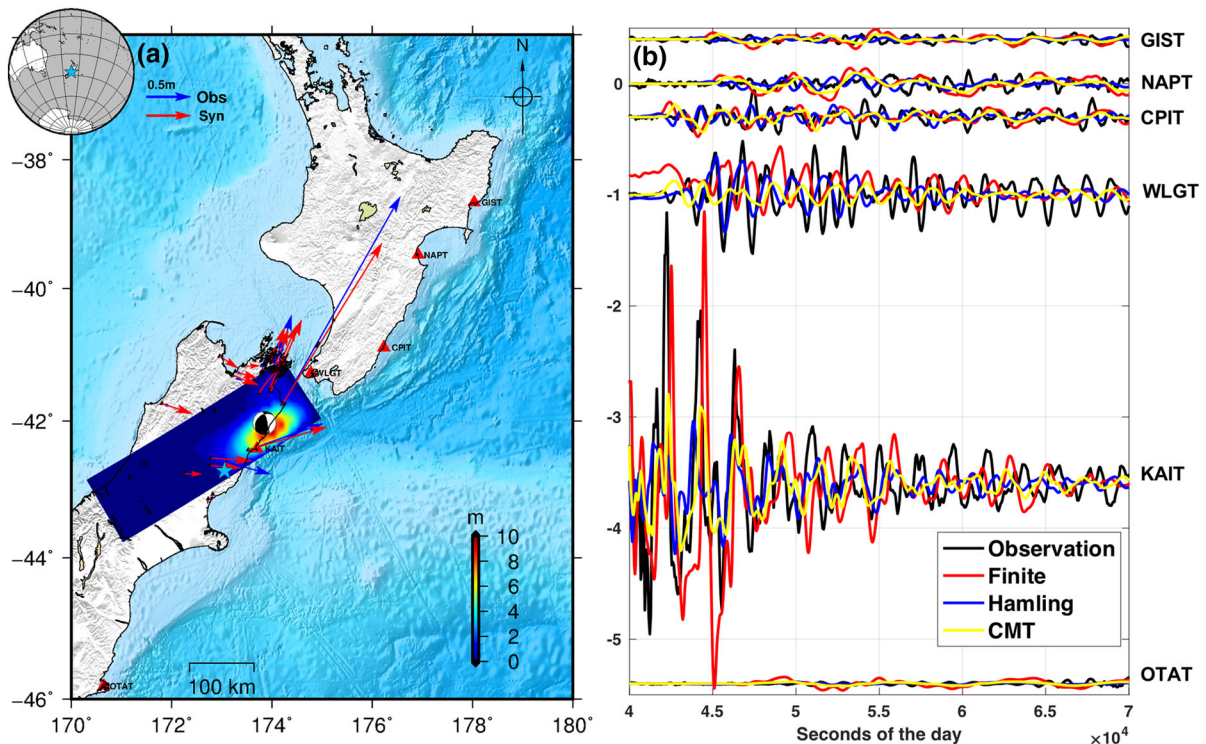

Figure 9
a Slip distribution inverted from a single fault plane for the 2016 New Zealand M_w 7.8 Kaikoura earthquake. USGS epicenter and GCMT solution are denoted by the blue star and black beachball, GNSS observations and fits, are shown by blue and red vectors, respectively. Tide gauges are indicated by red triangles. **b** The tsunami waves at six tide gauges. Black lines show observed wave amplitudes, red and blue are the predicted based our single fault model and multi-fault model provided by Hamling et al. (2017), yellow denotes predictions from the GCMT solution

the source complexities, it is still a good-enough average source that provides valuable constraints.

3.5. The 5 August 2018 M_w 7.0 Lombok Event

The 5 August 2018 near coast M_w 7.0 Lombok earthquake, which caused more than 560 deaths and triggered a tsunami warning, provided one recent example to test how our system responds in real-time case. Here we present a timeline of the response to this damaging earthquake in the context of tsunami early warning. This earthquake originated at 11:46:35 UTC, and USGS-NEIC released the preliminary epicenter location (10 km default depth) and magnitude (M_L 7.0) about 1 min later, which initialized the automatic finite source inversion on JPL's GATED system. In spite that the epicenter falls in the projection of Slab2, its hypocenter depth as 10 km was too far away from the Slab2 depth 144 km there, which excluded an inter-plate thrusting rupture, and we had to use interpolated focal mechanism: strike/ dip/rake either 90/21/96 or 264/69/88. Besides, the epicenter location indicated that there were no near-field GNSS stations available and the inversion had to rely on P waveforms at 10 teleseismic stations within 45° epicentral distance (see Fig. 10a). Once the two fault planes and station distribution were fixed, the computation of Green's functions and formation of normal equations began, which then took ∼ 9 min to be accomplished on a desktop computer. At the same time, the system waited for the arrival of P displacement waveforms. Theoretically, it would take ∼ 6 min for the P waves travelling to the nearest station PMG (with 30.37° epicentral distance) and ∼ 8 min to the furthest station TAU (with 43.96° epicentral distance). P waveforms were automatically collected for inversion at about 11 min after the earthquake origin. The preferable inversion result and corresponding surface deformation were obtained ∼ 13 min after the origin.

Moment magnitude of this event is M_w 7.0, data fits favor strike/dip/rake as 264/69/88 and are generally reasonable (see Fig. 10b, VR = 67%) and co-seismic slip distribution (see Fig. 10c) does not suggest a damaging tsunami because most of the ruptures are onshore. For this event, there is no publicly available tsunami data to evaluate the system

performance. Alternatively, we conduct a comparison between the synthetic surface deformation and the Sentinel-1 observations (Fig. 10d, e). While the predicted deformations are the same order of magnitude as InSAR observations, it seems that the teleseismic inversion does not produce the slip distribution at the same location as suggested by the Sentinel-1 measurements, which shows the major slip concentrate northwest of the epicenter. This discrepancy is probably a result of the inherent poor spatial resolution of P waves. Nonetheless, the rapid solution excludes the possibility of a devasting tsunami and is very helpful to the local authority for risk management in the first minutes.

4. Summary and Future Improvements

4.1. Summary

In this paper, we have demonstrated how the two real-time observational networks—GNSS and seismic—can be automated together to have a denser global coverage for earthquake finite-source inversion and for tsunami early warning. The main innovative part of this work is the successful implementation of the proposed inversion algorithm in real-time operation. Though many components of the algorithm have been available for years and published previously as cited in the reference, automating them into an operational system is actually difficult and time consuming. Particularly for earthquakes, which can occur anywhere and anytime, without a global coverage to capture a real event and an automated system to process the event day and night, an algorithm could not be tested sufficient and reliable for confident applications in real time. Our system is currently in operation, and will have more opportunities to gain experience in using GNSS and seismic data. Through a detailed analysis of the five recent tsunamigenic events, we find that our automated finite source inversion jointly using GNSS and teleseismic networks is more reliable and effective than using only one of the two networks for tsunami early warning.

Our main strategy is to take the advantages of near-field (epicentral distance < 1000 km) GNSS
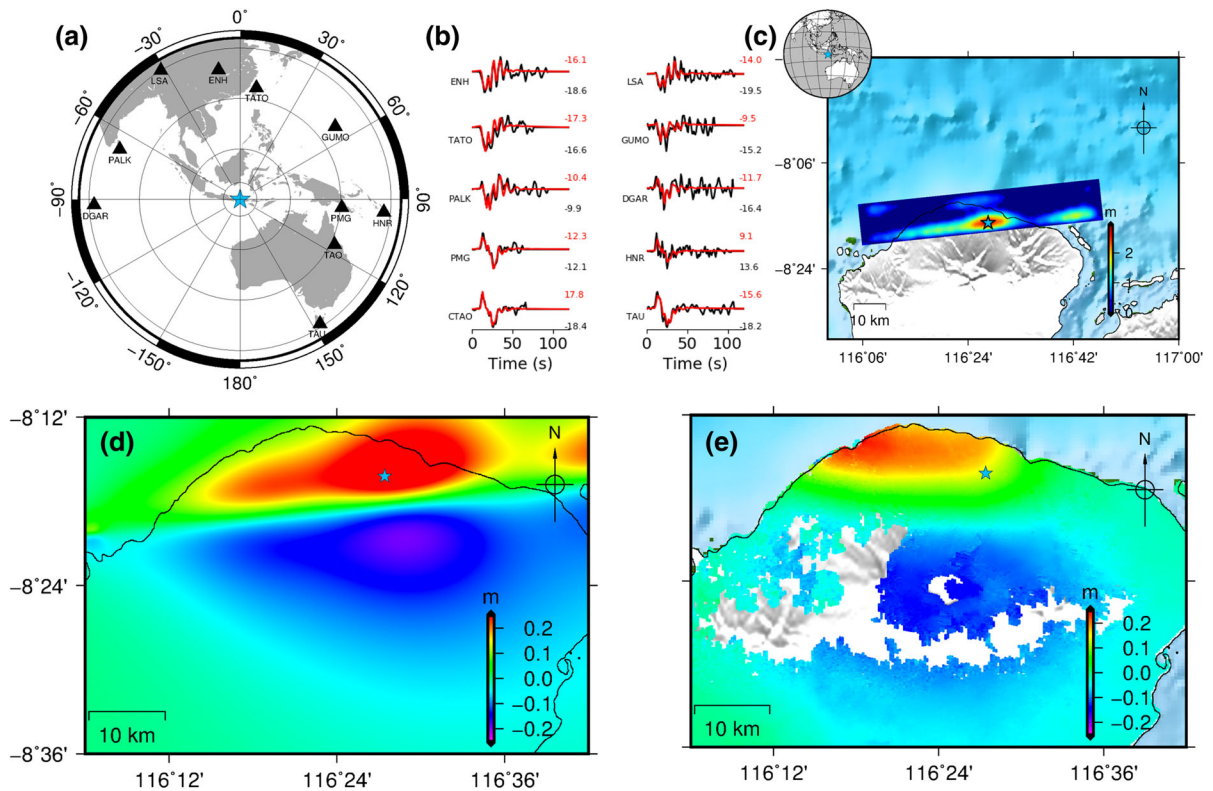
Figure 10
Summary of the 5 August 2018 Lombok event. **a** Distribution of teleseismic stations, blue star locates the epicenter. **b** Observations (in black) and synthetics (in red) of P displacement waveforms. **c** Map view of co-seismic slip distribution from teleseismic observations. **d** Synthetic line of sight deformation based on co-seismic slip distribution. **e** Sentineal-1 line of sight measurements between 30 July and 5 August, 2018

data and mid-range (epicentral distance from 30° to 45°) teleseismic P displacement waveforms for finite source inversion of large earthquakes. Neither the near-field GNSS nor the mid-range teleseismic data clip or saturate during large earthquakes, while the fast-traveling P-waves, within $6\sim8$ min away from the epicenter, are still essential to constrain the source in regions where GNSS data are not dense enough. Although many recent studies underscore the advantage of near-field GNSS for tsunami early warning through post-event studies, few applications using real-time GNSS have been reported in operational mode, partly due to its poor coverage and intrinsic accuracy. Jointly augmented with teleseismic data, our system not only takes the benefits of GNSS but also is now operational in real-time. To highlight our strategy, we re-analyzed all of the $M_w > 7.0$ shallow earthquakes (most are tsunamigenic subduction zone

earthquakes) from 1995 to the end of 2017 (see Fig. 11), and find that near-filed GNSS data are only available in certain regions; therefore, relying solely on GNSS data would not provide enough tsunami warning information at a global scale (Fig. 11a). By contrast, our system is able to get earthquake source characters within 10 min on a moderate desktop workstation (Fig. 11b: green and purple dots). The computational time will certainly be reduced significantly once the system is matured and ported to parallel high-performance computing systems.

4.2. Future improvements

Clearly, rapid and reliable finite earthquake source inversion is a central part of our ongoing efforts to improve the robustness of tsunami early warning. However, finite source inversion is
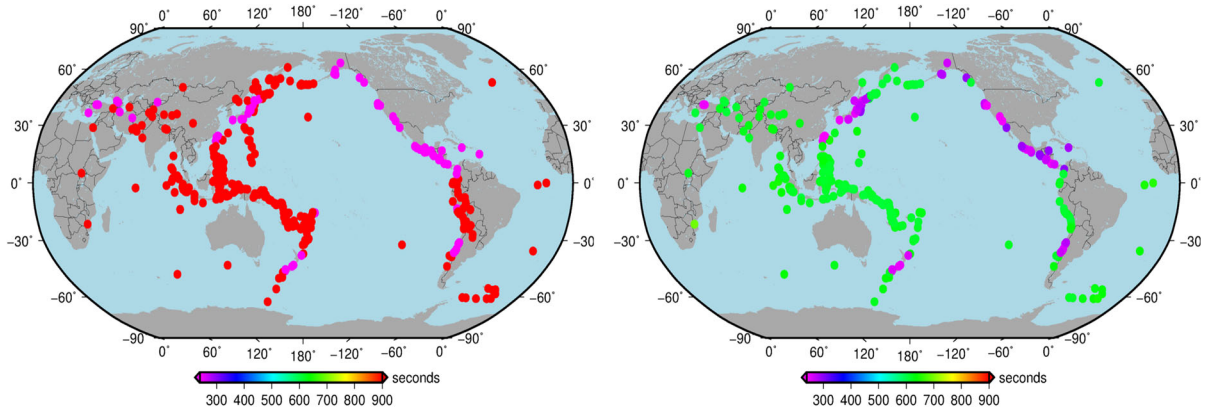
Figure 11

Time needed for earthquake source inversion: (right) using GNSS data only, and (left) using both GNSS and teleseismic data. The synthetic test is for $M_w > 7.0$ earthquakes (color dots on the map) since 1990. The color bar is saturated and > 900 s in right panel means we will never have a solution

inherently ill-posed (Ide 2015). Worse still, due to limited datasets, rapid finite source inversion is subject to even larger uncertainty. To this end, our future work will focus on adopting more real-time datasets and indicating inversion reliability.

Compared with static GNSS offsets, high-rate GNSS displacement waveforms contain timing information of local rupture propagation and can help constrain temporal resolution. What's more, GNSS displacement waveforms have the potential to improve near-trench resolution by reconciling with the depth-dependent megathrust rupture behaviors (Yue and Lay 2011). However, data loss and discontinuity in current high-rate GNSS can be problematic for waveforms in real time. Although the problem will be resolved with the advances in telecommunications, in current situation, the joint GNSS and seismic waveforms inversion is a better strategy for more reliable solutions.

Regional accelerogram waveforms are also suggested to increase the resolution of the slip distribution for large earthquakes and for moderate earthquakes (Chen et al. 2018). Recently, accelerator data have been archived by several large regional networks for public access, such as K-NET and KiK-net (http://www.kyoshin.bosai.go.jp) in Japan, California Strong Motion Instrumentation Program (http://www.consrv.ca.gov/cgs/smip) in United States. However, they are even more sparse than the GNSS data. Co-located with GNSS stations are few. We have gained some experience in using accelerogram waveforms in a moderate earthquake (Chen et al. 2018) and are looking forward to including the strong motion data into our system too.

Jointly using tsunami data for earthquake inversion has also been widely reported in literature. For example, Fujii et al. (2011) found that tsunami data could be used to constrain slip inversions and improve the resolution of near-trench shallow slip. By joint inversion of onshore GNSS data and offshore buoys, Melgar and Bock (2015) demonstrated that the source of 2011 M_w 9.0 Tohoku event can be better imaged which enhances the prediction of tsunami inundation and runup. However, most of the studies using tsunami data are after-event demonstration. Obtaining tsunami data has to wait for the tsunami to pass the observed location. In many cases, it is too late for near-field early warning, which is the focus of tsunami early warning in practice. In addition, the tsunami data inversion is subject to the assumption of the tsunami formation theory, which is a research topic that deserves further study.

A direct evaluation of the uncertainty of the slip model remains challenging since the true source is always unknown for a natural earthquake. While our system does not provide the uncertainty of inverted slip models currently, we acknowledge that there are some epistemic uncertainties which can affect the

reliability of the models. For example, there are generally two types of tsunamigenic earthquakes: earthquakes at the plate interface (inter-plate subduction megathrust events), earthquakes at the outer rise, within the subducting slab or overlying crust (intra-plate events). While in most cases the assumption of thrust earthquake is reasonable when an earthquake happens in the coverage of Slab2 and its hypocenter depth is within 30 km of the Slab2 depth as set by our system, due to the relatively poor accuracy of the initial hypocenter depth, there is the possibility that it can be an intra-slab or outer rise normal faulting earthquake (e.g., the 2017 Mexico Tehuantepec M_w 8.2 event), which will lead to poor data fits because of a wrong focal mechanism adopted. Moreover, because teleseismic P waves have low resolution on the absolute location, slip location based on teleseismic P waves may be shifted due to the inaccuracy of an initial epicentral determination as shown in 5 August 2018 M_w 7.0 Lombok event. More research would be needed in this area.

We strongly believe that the research and improvements would be more effective by testing new methods and data in a real-time system, then carefully validating the results after event. With our algorithm implemented in the real-time system, we would have more chances to test it through real events, either large or moderate earthquakes. Our follow-up study will report the real-time performance and uncertainty statistics from the application of our algorithm to more real events.

Acknowledgements

Publisher's Note Springer Nature remains neutral with regard to jurisdictional claims in published maps and institutional affiliations.

REFERENCES

Akaike, H. (1980). Likelihood and the Bayes procedure. *Trabajos de estadistica y de investigacion operativa, 31*(1), 143–166. https://doi.org/10.1007/BF02888350.

Ammon, C. J., Kanamori, H., Lay, T., & Velasco, A. A. (2006). The 17 July 2006 Java tsunami earthquake. *Geophysical Research Letters, 33*(24), 1–5. https://doi.org/10.1029/2006GL028005.

Babeyko, A. Y., Hoechner, A., & Sobolev, S. V. (2010). Source modeling and inversion with near real-time GPS: A GITEWS perspective for Indonesia. *Natural Hazards and Earth Systems Sciences, 10*(7), 1617–1627. https://doi.org/10.5194/nhess-10-1617-2010.

Báez, J. C., et al. (2018). The Chilean GNSS network: Current status and progress toward early warning applications. *Seismological Research Letters, 166,* 29–65. https://doi.org/10.1785/0220180011.

Bai, Y., Lay, T., Cheung, K. F., & Ye, L. (2017). Two regions of seafloor deformation generated the tsunami for the 13 November 2016, Kaikoura, New Zealand earthquake. *Geophysical Research Letters.* https://doi.org/10.1002/2017gl073717.

Becker, J. J., et al. (2009). Global bathymetry and elevation data at 30 arc seconds resolution: SRTM30_PLUS. *Marine Geodesy, 32*(4), 355–371. https://doi.org/10.1080/01490410903297766.

Bernard, E., & Titov, V. (2015). Evolution of tsunami warning systems and products. *Philosophical Transactions of the Royal Society A: Mathematical, Physical and Engineering Sciences., 373*(2053), 20140371. https://doi.org/10.1098/rsta.2014.0371.

Bilek, S. L., & Lay, T. (1999). Rigidity variations with depth along interplate megathrust faults in subduction zones. *Nature, 400*(6743), 443–446. https://doi.org/10.1038/22739.

Blewitt, G., Kreemer, C., Hammond, W. C., Plag, H.-P., Stein, S., & Okal, E. (2006). Rapid determination of earthquake magnitude using GPS for tsunami warning systems. *Geophysical Research Letters, 33*(11), L11309. https://doi.org/10.1029/2006GL026145.

Boatwright, J., & Choy, G. L. (1986). Teleseismic estimates of the energy radiated by shallow earthquakes. *Journal of Geophysical Research, 91*(B2), 2095. https://doi.org/10.1029/JB091iB02p02095.

Bock, Y., Nikolaidis, R. M., de Jonge, P. J., & Bevis, M. (2000). Instantaneous geodetic positioning at medium distances with the Global Positioning System. *Journal of Geophysical Research, 105*(B12), 28223. https://doi.org/10.1029/2000jb900268.

Chen, K., Babeyko, A., Hoechner, A., & Ge, M. (2016a). Comparing source inversion techniques for GPS-based local tsunami forecasting: A case study for the April 2014M 8.1 Iquique, Chile, earthquake. *Geophysical Research Letters, 43*(7), 3186–3192. https://doi.org/10.1002/2016gl068042.

Chen, K., Ge, M., Babeyko, A., Li, X., Diao, F., & Tu, R. (2016b). Retrieving real-time co-seismic displacements using GPS/GLONASS: A preliminary report from the September 2015 Mw 8.3 Illapel earthquake in Chile. *Geophysical Journal International, 206*(2), 941–953. https://doi.org/10.1093/gji/ggw190.

Chen, K., Liu, Z., Liang, C., & Song, Y. T. (2018). Towards the application of seismogeodesy in central Italy: A case study for the 2016 August 24 Mw 6.1 Italy earthquake modelling. *Geophysical Journal International, 213*(3), 1647–1658. https://doi.org/10.1093/gji/ggy089.

Contreras-López, M., et al. (2016). Field survey of the 2015 Chile tsunami with emphasis on coastal wetland and conservation areas. *Pure and Applied Geophysics, 173*(2), 349–367. https://doi.org/10.1007/s00024-015-1235-2.

Crowell, B. W., Bock, Y., & Melgar, D. (2012). Real-time inversion of GPS data for finite fault modeling and rapid hazard assessment. *Geophysical Research Letters*. https://doi.org/10.1029/2012gl051318.

Duputel, Z., Rivera, L., Kanamori, H., Hayes, G. P., Hirshorn, B., & Weinstein, S. (2011). Real-time W phase inversion during the 2011 off the Pacific coast of Tohoku Earthquake. *Earth, Planets and Space, 63*(7), 535–539. https://doi.org/10.5047/eps.2011.05.032.

Dziewonski, A. M., & Anderson, D. L. (1981). Preliminary reference earth model. *Physics of the Earth and Planetary Interiors, 25*(4), 297–356. https://doi.org/10.1016/0031-9201(81)90046-7.

Fujii, Y., Satake, K., Sakai, S., Shinohara, M., & Kanazawa, T. (2011). Tsunami source of the 2011 off the Pacific coast of Tohoku Earthquake. *Earth, Planets and Space, 63*(7), 815–820. https://doi.org/10.5047/eps.2011.06.010.

Fu, Y., Song, Y. T., & Gross, R. S. (2017). Linking oceanic tsunamis and geodetic gravity changes of large earthquakes. *Pure and Applied Geophysics, 174*(8), 3029–3041. https://doi.org/10.1007/s00024-017-1510-5.

Geng, J., Jiang, P., & Liu, J. (2017). Integrating GPS with GLONASS for high-rate seismogeodesy. *Geophysical Research Letters*. https://doi.org/10.1002/2017gl072808.

Hamling, I. J., et al. (2017). Complex multifault rupture during the 2016 M w 7.8 Kaikōura earthquake, New Zealand. *Science*. https://doi.org/10.1126/science.aam7194.

Hartzell, S. H., & Heaton, T. H. (1983). Inversion of strong ground motion and teleseismic waveform data for the fault rupture history of the 1979 Imperial Valley, California, earthquake. *Bulletin of the Seismological Society of America, 73*(6), 1553–1583.

Hayes, G. P., Earle, P. S., Benz, H. M., Wald, D. J., & Briggs, R. W. (2011). 88 hours: The U.S. Geological survey national earthquake information center response to the 11 March 2011 Mw 9.0 Tohoku earthquake. *Seismological Research Letters, 82*(4), 481–493. https://doi.org/10.1785/gssrl.82.4.481.

Hayes, G. P., Moore, G. L., Portner, D. E., Hearne, M., Flamme, H., Furtney, M., et al. (2018). Slab2, a comprehensive subduction zone geometry model. *Science (80-.)*. https://doi.org/10.1126/science.aat4723.

Hayes, G. P., & Wald, D. J. (2009). Developing framework to constrain the geometry of the seismic rupture plane on subduction interfaces a priori—A probabilistic approach. *Geophysical Journal International, 176*(3), 951–964. https://doi.org/10.1111/j.1365-246X.2008.04035.x.

Hayes, G. P., Wald, D. J., & Johnson, R. L. (2012). Slab1.0: A three-dimensional model of global subduction zone geometries. *Journal of Geophysical Research: Solid Earth, 117*(1), 1–15. https://doi.org/10.1029/2011jb008524.

Hirshorn, B., Weinstein, S., & Tsuboi, S. (2013). On the application of Mwp in the near field and the March 11, 2011 Tohoku Earthquake. *Pure and Applied Geophysics, 170*(6–8), 975–991. https://doi.org/10.1007/s00024-012-0495-3.

Hoshiba, M., Iwakiri, K., Hayashimoto, N., Shimoyama, T., Hirano, K., Yamada, Y., et al. (2011). Outline of the 2011 off the Pacific coast of Tohoku Earthquake (M w 90)—Earthquake Early Warning and observed seismic intensity. *Earth, Planets and Space, 63*(7), 547–551. https://doi.org/10.5047/eps.2011.05.031.

Husen, S., & Hardebeck, J. (2010). Earthquake location accuracy. *Community Online Resource Static Seismic Analysis*. https://doi.org/10.5078/corssa-55815573.

Ide, S. (2015). Slip inversion. In G. C. Beroza, & H. Kanamori, (Eds.), *Earthquake Seismology, Treatise on Geophysics* (vol. 4, pp. 215–241). Elsevier: Amsterdam, The Netherlands.

Ide, S., Takeo, M., & Yoshida, Y. (1996). Source process of the 1995 kobe earthquake: Determination of spatio-temporal slip distribution by bayesian modeling. *Bulletin of the Seismological Society of America, 86*(3), 547–566.

Inazu, D., Pulido, N., Fukuyama, E., Saito, T., Senda, J., & Kumagai, H. (2016). Near-field tsunami forecast system based on near real-time seismic moment tensor estimation in the regions of Indonesia, the Philippines, and Chile 4. *Seismology, Earth, Planets and Space*. https://doi.org/10.1186/s40623-016-0445-x.

JMA. (2013). Lessons learned from the tsunami disaster caused by the 2011 Great East Japan Earthquake and improvements in JMA's tsunami warning system. http://www.data.jma.go.jp/svd/eqev/data/en/tsunami/LessonsLearned_Improvements_brochure.pdf.

Kagan, Y. Y. (1991). Correlations of earthquake focal mechanisms. *Geophysical Journal International, 143*(3), 881–897. https://doi.org/10.1046/j.1365-246X.2000.00281.x.

Kagan, Y. Y., & Jackson, D. D. (1994). Long-term probabilistic forecasting of earthquakes. *Journal of Geophysical Research, 99*(B7), 13613–685700. https://doi.org/10.1029/94jb00500.

Kanamori, H. (1972). Mechanism of tsunami earthquakes. *Physics of the Earth and Planetary Interiors, 6*(5), 346–359. https://doi.org/10.1016/0031-9201(72)90058-1.

Kanamori, H. (1977). The energy release in great earthquakes. *Journal of Geophysical Research, 82*(20), 2981–2987. https://doi.org/10.1029/JB082i020p02981.

Kanamori, H., & Rivera, L. (2008). Source inversion of W phase: Speeding up seismic tsunami warning. *Geophysical Journal International, 175*(1), 222–238. https://doi.org/10.1111/j.1365-246X.2008.03887.x.

Kawamoto, S., Hiyama, Y., Ohta, Y., & Nishimura, T. (2016). First result from the GEONET real-time analysis system (REGARD): The case of the 2016 Kumamoto earthquakes. *Earth, Planets and Space*. https://doi.org/10.1186/s40623-016-0564-4.

Kawamoto, S., Ohta, Y., Hiyama, Y., Todoriki, M., Nishimura, T., Furuya, T., et al. (2017). REGARD: A new GNSS-based real-time finite fault modeling system for GEONET. *Journal of Geophysical Research: Solid Earth, 122*(2), 1324–1349. https://doi.org/10.1002/2016JB013485.

Kikuchi, M., & Kanamori, H. (1982). Inversion of complex body waves. *Bulletin of the Seismological Society of America, 72*(2), 491–506.

Kubo, A., Fukuyama, E., Kawai, H., & Nonomura, K. (2002). NIED seismic moment tensor catalogue for regional earthquakes around Japan: Quality test and application. *Tectonophysics, 356*(1–3), 23–48. https://doi.org/10.1016/S0040-1951(02)00375-X.

Larson, K. M., Bodin, P., & Gomberg, J. (2003). Using 1-Hz GPS data to measure deformations caused by the Denali fault earthquake. *Science, 300*(5624), 1421–1424. https://doi.org/10.1126/science.1084531.

Li, X., Ge, M., Guo, B., Wickert, J., & Schuh, H. (2013). Temporal point positioning approach for real-time GNSS seismology using a single receiver. *Geophysical Research Letters, 40*(21), 5677–5682. https://doi.org/10.1002/2013GL057818.

Liu, Z., Owen, S., & Moore, A. (2014). Rapid estimate and modeling of permanent coseismic displacements for large earthquakes using high-rate global positioning system data. *Seismological Research Letters, 85*(2), 284–294. https://doi.org/10.1785/0220130174.

MacInnes, B. T., Gusman, A. R., LeVeque, R. J., & Tanioka, Y. (2013). Comparison of earthquake source models for the 2011 Tohoku event using tsunami simulations and near-field observations. *Bulletin of the Seismological Society of America, 103*(2B), 1256–1274. https://doi.org/10.1785/0120120121.

Melgar, D., & Bock, Y. (2015). Kinematic earthquake source inversion and tsunami runup prediction with regional geophysical data. *Journal of Geophysical Research: Solid Earth, 120*(5), 3324–3349. https://doi.org/10.1002/2014JB011832.

Melgar, D., Bock, Y., & Crowell, B. W. (2012). Real-time centroid moment tensor determination for large earthquakes from local and regional displacement records. *Geophysical Journal International, 188*(2), 703–718. https://doi.org/10.1111/j.1365-246X.2011.05297.x.

Melgar, D., LeVeque, R. J., Dreger, D. S., & Allen, R. M. (2016). Kinematic rupture scenarios and synthetic displacement data: An example application to the Cascadia subduction zone. *Journal of Geophysical Research: Solid Earth, 121*(9), 6658–6674. https://doi.org/10.1002/2016JB013314.

Mendoza, C., & Hartzell, S. (2013). Finite-fault source inversion using teleseismic P waves: Simple parameterization and rapid analysis. *Journal of Geophysical Research: Solid Earth, 103*(2A), 834–844. https://doi.org/10.1785/0120120069.

Mori, N., Takahashi, T., Yasuda, T., & Yanagisawa, H. (2011). Survey of 2011 Tohoku earthquake tsunami inundation and run-up. *Geophysical Research Letters*. https://doi.org/10.1029/2011gl049210.

Okada, Y. (1985). Surface deformation due to shear and tensile faults in a half-space. *Bulletin of the Seismological Society of America, 75*(4), 1135–1154.

Ohta, Y., Kobayashi, T., Tsushima, H., Miura, S., Hino, R., Takasu, T., et al. (2012). Quasi real-time fault model estimation for near-field tsunami forecasting based on RTK-GPS analysis: application to the 2011 Tohoku-Oki earthquake (Mw 9.0). *Journal of Geophysical Research, 117*, B02311. https://doi.org/10.1029/2011JB008750.

Okuwaki, R., Yagi, Y., Aránguiz, R., González, J., & González, G. (2016). Rupture Process During the 2015 Illapel, Chile Earthquake: Zigzag-Along-Dip Rupture Episodes. *Pure and Applied Geophysics*. https://doi.org/10.1007/s00024-016-1271-6.

Richter, C. F. (1935). An instrumental earthquake magnitude scale. *Bulletin of the Seismological Society of America, 25,* 1–32.

Riquelme, S., Bravo, F., Melgar, D., Benavente, R., Geng, J., Barrientos, S., et al. (2016). W phase source inversion using high-rate regional GPS data for large earthquakes. *Geophysical Research Letters, 43*(7), 3178–3185. https://doi.org/10.1002/2016GL068302.

Sobolev, S. V., Babeyko, A. Y., Wang, R., Hoechner, A., Galas, R., Rothacher, M., et al. (2007). Tsunami early warning using GPS-Shield arrays. *Journal of Geophysical Research, 112*(B8), B08415. https://doi.org/10.1029/2006JB004640.

Song, Y. T. (2007). Detecting tsunami genesis and scales directly from coastal GPS stations. *Geophysical Research Letters, 34*(19), L19602. https://doi.org/10.1029/2007GL031681.

Song, Y. T., Fu, L. L., Zlotnicki, V., Ji, C., Hjorleifsdottir, V., Shum, C. K., et al. (2008). The role of horizontal impulses of the faulting continental slope in generating the 26 December 2004 tsunami. *Ocean Modelling, 20*(4), 362–379. https://doi.org/10.1016/j.ocemod.2007.10.007.

Song, Y. T., Fukumori, I., Shum, C. K., & Yi, Y. (2012). Merging tsunamis of the 2011 Tohoku-Oki earthquake detected over the open ocean. *Geophysical Research Letters*. https://doi.org/10.1029/2011gl050767.

Song, Y. T., Mohtat, A., & Yim, S. C. (2017). New insights on tsunami genesis and energy source. *Journal of Geophysical Research: Oceans*. https://doi.org/10.1002/2016jc012556.

Tanioka, Y., & Satake, K. (1996). Tsunami generation by horizontal displacement of ocean bottom. *Geophysical Research Letters, 23*(8), 861–864. https://doi.org/10.1029/96GL00736.

Tappin, D. R., Grilli, S. T., Harris, J. C., Geller, R. J., Masterlark, T., Kirby, J. T., et al. (2014). Did a submarine landslide contribute to the 2011 Tohoku tsunami? *Marine Geology, 357,* 344–361. https://doi.org/10.1016/j.margeo.2014.09.043.

Titov, V. V., Gonzalez, F. I., Bernard, E. N., Eble, M. C., Mofjeld, H. O., Newman, J. C., et al. (2005). Real-time tsunami forecasting: Challenges and solutions. *Natural Hazards, 35*(1), 35–41. https://doi.org/10.1007/s11069-004-2403-3.

Titov, V. V, Mofjeld, H. O., & González, F. I. (1999). Offshore forecasting of Hawaiian tsunamis generated in Alaskan-Aleutian subduction zone, *NOAA Tech*.

Titov, V., Song, Y. T., Tang, L., Bernard, E. N., Bar-Sever, Y., & Wei, Y. (2016). Consistent estimates of tsunami energy show promise for improved early warning. *Pure and Applied Geophysics, 173*(12), 3863–3880. https://doi.org/10.1007/s00024-016-1312-1.

Weinstein, S. A., & Lundgren, P. R. (2008). Finite fault modeling in a tsunami warning center context. *Pure and Applied Geophysics, 165*(3–4), 451–474. https://doi.org/10.1007/s00024-008-0316-x.

Wells, D. L., & Coppersmith, K. J. (1994). New empirical relationships among magnitude, rupture length, rupture width, rupture area, and surface displacement. *Bulletin of the Seismological Society of America, 84*(4), 974–1002.

Yang, Y.-M., Meng, X., Komjathy, A., Verkholyadova, O., Langley, R. B., Tsurutani, B. T., et al. (2014). Tohoku-Oki earthquake caused major ionospheric disturbances at 450 km altitude over Alaska. *Radio Science, 49*(12), 1206–1213. https://doi.org/10.1002/2014RS005580.

Yue, H., & Lay, T. (2011). Inversion of high-rate (1 sps) GPS data for rupture process of the 11 March 2011 Tohoku earthquake

(Mw 9.1). *Geophysical Research Letters, 38,* L00G09. https://doi.org/10.1029/2011gl048700.

Yue, H., & Lay, T. (2013). Source Rupture Models for the Mw 9.0 2011 Tohoku Earthquake from Joint Inversions of High-Rate Geodetic and Seismic Data. *Bulletin of the Seismological Society of America, 103*(2B), 1242–1255. https://doi.org/10.1785/0120120119.

Yue, H., Lay, T., Rivera, L., Bai, Y., Yamazaki, Y., Cheung, K. F., et al. (2014). Rupture process of the 2010 M w 7.8 Mentawai tsunami earthquake from joint inversion of near-field hr-GPS and teleseismic body wave recordings constrained by tsunami observations. *Journal of Geophysical Research: Solid Earth, 119*(7), 5574–5593. https://doi.org/10.1002/2014jb011082.

Zhu, L., & Rivera, L. A. (2002). A note on the dynamic and static displacements from a point source in multilayered media. *Geophysical Journal International, 148*(3), 619–627. https://doi.org/10.1046/j.1365-246X.2002.01610.x.